



HAL
open science

Optimal choice of closest approach distance for a comet flyby: Application to the Comet Interceptor mission

J. de Keyser, N. J. T. Edberg, P. Henri, H. Rothkaehl, V. Della Corte, M. Rubin, R. Funase, S. Kasahara, C. Snodgrass

► To cite this version:

J. de Keyser, N. J. T. Edberg, P. Henri, H. Rothkaehl, V. Della Corte, et al.. Optimal choice of closest approach distance for a comet flyby: Application to the Comet Interceptor mission. Planetary and Space Science, 2025, 256, 10.1016/j.pss.2024.106032 . insu-04909657

HAL Id: insu-04909657

<https://insu.hal.science/insu-04909657v1>

Submitted on 24 Jan 2025

HAL is a multi-disciplinary open access archive for the deposit and dissemination of scientific research documents, whether they are published or not. The documents may come from teaching and research institutions in France or abroad, or from public or private research centers.


L'archive ouverte pluridisciplinaire **HAL**, est destinée au dépôt et à la diffusion de documents scientifiques de niveau recherche, publiés ou non, émanant des établissements d'enseignement et de recherche français ou étrangers, des laboratoires publics ou privés.



Distributed under a Creative Commons Attribution - NonCommercial - NoDerivatives 4.0 International License



Optimal choice of closest approach distance for a comet flyby: Application to the Comet Interceptor mission

J. De Keyser^{a,b}^{*}, N.J.T. Edberg^c, P. Henri^{d,e}, H. Rothkaehl^f, V. Della Corte^g, M. Rubin^h, R. Funaseⁱ, S. Kasahara^j, C. Snodgrass^k

^a Space Physics Division, Royal Belgian Institute for Space Aeronomy (BIRA-IASB), Ringlaan 3, B-1180, Brussels, Belgium

^b Center for mathematical Plasma Astrophysics, Katholieke Universiteit Leuven, Celestijnenlaan 200B, B-3001, Heverlee, Belgium

^c Swedish Institute of Space Physics (IRF), Uppsala, Sweden

^d Laboratoire de Physique et Chimie de l'Environnement et de l'Espace (LPC2E), CNRS, Orléans, France

^e Laboratoire Lagrange, Observatoire de la Côte d'Azur, Université Côte d'Azur (OCA), CNRS, Nice, France

^f CBK, Polish Academy of Sciences, Warsaw, Poland

^g INAF – Osservatorio Astronomico di Capodimonte, Napoli, Italy

^h Space Research and Planetary Sciences, Physikalisches Institut, Universität Bern, Bern, Switzerland

ⁱ Japan Aerospace Exploration Agency, Institute of Space and Astronautical Science, Sagami-hara, Japan

^j Department of Earth and Planetary Science, The University of Tokyo, Tokyo, Japan

^k Institute for Astronomy, University of Edinburgh, Royal Observatory, Edinburgh, UK

ARTICLE INFO

Dataset link: <https://doi.org/10.18758/nn9g6vno>

Keywords:

Comet flyby mission design
Comet dust impact risk
Comet Interceptor

ABSTRACT

A comet flyby, like the one planned for the Comet Interceptor mission, takes place under conditions that remain largely unknown up to the moment of encounter. A detailed trajectory design phase, which includes verification of the technical limitations implied by the flyby geometry, precedes target comet selection. Thus the flyby velocity and the solar zenith angle at closest approach are known in advance. Solar irradiance and the neutral gas expansion speed can be estimated reasonably well. However, the comet outgassing rate, the dust production rate, and the solar wind conditions are only known within broader uncertainty margins. The present paper aims to optimally choose the one degree of freedom that is available for tuning the flyby conditions: the distance of closest approach. This choice is based on a simplified formalism that expresses, on one hand, the science return to be expected as a function of the closest approach distance, and, on the other hand, the risks implied by a close approach. This is done by performing Monte Carlo simulations over a large sample of possible comet flyby configurations, based on the expected probability distributions of the gas and dust production rates and the solar wind conditions, for different closest approach distances. For small flyby distances, a spacecraft has the opportunity to study the nucleus, the neutral gas coma, and the induced magnetosphere from up close, benefiting the science return. There is a trade-off to be made against the cometary dust collision risk, which becomes larger close to the nucleus. This trade-off is illustrated for the case of the Comet Interceptor main spacecraft and the two probes it plans to release. The change of the optimal flyby distance with gas and dust production rate, solar EUV flux, and flyby speed is discussed.

1. Introduction

Apart from the European Space Agency's (ESA's) Rosetta mission (Taylor et al., 2015), comet exploration has been conducted with flybys. The most notable ones visited 1P/Halley, with the Giotto spacecraft passing at ~600 km distance from the nucleus, and Vega 1 and 2, Suisei, and Sakigake farther out (Reinhard, 1986). Other flybys include Giotto's passage past 26P/Grigg-Skjellerup (Morley, 1991; McDonnell et al., 1993), Deep Space 1 at 19P/Borrelly (Boice et al.,

2000), ICE at 21P/Giacobini-Zinner (Brandt et al., 1985), Stardust at 81P/Wild 2 (Brownlee et al., 2006) and at 9P/Tempel (Veverka et al., 2013), and Deep Impact at 9P/Tempel (A'Hearn et al., 2005) and at 103P/Hartley2 (A'Hearn et al., 2011). Despite the short period during which scientific measurements of the comet environment can be made, a flyby allows to study these intriguing objects at a limited cost.

Preparations are currently underway for Comet Interceptor (CI), an F-class mission in the ESA Science Programme, that will attempt a flyby of a long-period comet, ideally a dynamically new one (Snodgrass and

* Corresponding author at: Space Physics Division, Royal Belgian Institute for Space Aeronomy (BIRA-IASB), Ringlaan 3, B-1180, Brussels, Belgium.
E-mail address: Johan.DeKeyser@aeronomie.be (J. De Keyser).

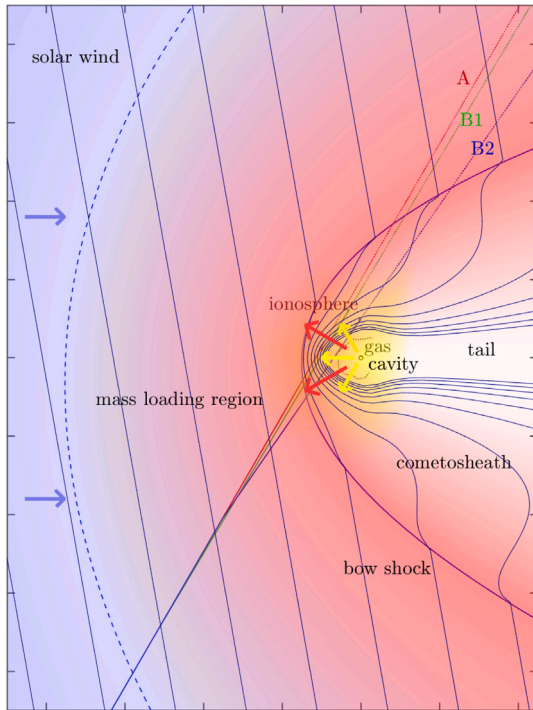


Fig. 1. Sketch of the structure of a comet magnetosphere and a typical Comet Interceptor flyby geometry (dimensions not to scale). The Sun is to the left. Probe B1 and later B2 are released from S/C A some time before the flyby. The figure presents a projection onto the ecliptic plane; the trajectories will not all lie in the same plane.

Jones, 2019; Jones et al., 2024). It consists of a main spacecraft (S/C A) that serves as a data relay and as an observing platform that stays rather far away from the nucleus, while two small probes (S/C B1 provided by the Japan Aerospace Exploration Agency, B2 by ESA) take more risk and will venture closer to the nucleus (Jones et al., 2024).

The flyby geometry is sketched in Fig. 1. Neutral gas from sublimation of ices on the nucleus forms an expanding comet atmosphere or gas coma, with a gas speed in the order of 1 km s^{-1} near 1 au. This gas is ionized by various mechanisms, forming a dense ionosphere. As soon as neutral cometary molecules are ionized in the solar wind region, they start gyrating around the interplanetary magnetic field. This “pick-up” phenomenon effectively deflects and slows down the solar wind, a process known as mass-loading. The supersonic and super-Alfvénic solar wind forms a bow shock upstream of the ionosphere. The shocked solar wind interaction with the ionosphere creates a diamagnetic cavity, within which the magnetic field vanishes. Magnetic field lines drape around the comet ionosphere and extend into the comet plasma tail (Goetz et al., 2022). At the same time, dust embedded in the sublimating ice is set free. Gas drag accelerates the dust particles until the expanding gas density and the corresponding drag have become negligible; dust terminal speeds therefore depend on dust mass and size but usually are small (in the order of m/s). Some dust particles may remain gravitationally trapped around the nucleus. The dynamics of very fine dust is influenced by solar radiation pressure. The dust coma extends into a comet dust tail in which the largest particles follow Keplerian orbits similar to that of the comet.

The CI flyby will take place near the ecliptic plane, between 0.9 and 1.2 au (Snodgrass and Jones, 2019), with flyby speed between 10 and 70 km s^{-1} (Jones et al., 2024). S/C A intends to release probe B1 38 h before closest approach (CA) and B2 20 h before CA (these times are subject to change as the mission operations plan is not definitive yet). After release, the probes drift away from S/C A. They are switched on upon release and remain active either until the S/C battery is depleted (for B2) or until their distance from S/C A becomes too large for the

inter-satellite link (ISL) via which the probes transmit their telemetry (for B1 and B2). The ISL is required to last until at least 3 h after CA, essentially until the end of life of B2. It is assumed here that the ISL is able to maintain contact with B1 throughout the entire encounter.

The target comet is selected before launch or during the early stages of the mission (Jones et al., 2024). In either case, the flyby parameters are known at least several months before the encounter. The only mission design parameter that can be tuned (within certain limits) is the closest approach distance R_{CA} . For the probes, the flyby distances depend on their speed relative to S/C A as well as on their release times, which are constrained by the probe lifetimes. The nominal CA distances are 1000, 850, and 400 km for S/C A, B1, and B2, respectively (Jones et al., 2024). It is important to adapt these values to the expected comet properties to maximize the scientific output, while at the same time limiting the risks associated with comet dust impacts. This is a choice that can typically be deferred until a few months or weeks before the encounter, allowing time to verify the technical feasibility of the flyby timeline, while the trajectory correction manoeuvres to fine-tune the flyby distance continue up to days before CA. The present paper describes a methodology for making this decision. Section 2 introduces a formalism for quantifying the science return and the dust impact risk. Section 3 explains how a trade-off between science return and risk can be made. The result of this analysis is reported in Section 4 for different conditions. The paper concludes with a discussion.

2. Science return and risks

Describing the science return of a mission that carries many instruments in an exhaustive and quantitative manner is beyond the scope of this work. Instead, a simplified approach is proposed in which each type of observation is described by a quantity q that indicates the quality of that kind of observation. Let q^* denote the nominal value for which one would consider the science return “as expected”. The science return is then evaluated as

$$\phi(q/q^*) = 1 - e^{-q/q^*}, \quad (1)$$

which is constructed to map a broad range of q/q^* values onto $[0, 1]$. For small q , the science return grows with q as any measurement is relevant. If $q = q^*$, the science return is 0.63, which corresponds to the nominal value. When $q > q^*$, the science return approaches 1 as it exceeds original expectations. As an example, the different types of comet observations made by CI are described in more detail below. For the reader’s convenience, the notation is summarized in Table 1.

CI originally envisaged an encounter with a dynamically new comet with high activity (Jones et al., 2019; Snodgrass and Jones, 2019). 1P/Halley-like activity would correspond to $Q_{\text{gas}} \approx 5 \times 10^{29}$ molecules s^{-1} at 1 au (Krankowsky et al., 1986). Chances that CI will encounter a comet with such an activity level, however, appear to be slim (De Keyser et al., 2024). Therefore, a comet activity $Q_{\text{gas}}^* \approx 5 \times 10^{28}$ molecules s^{-1} at 1 au is used here as a reference instead. Comet surveys show that such a gas production rate is not unusual (e.g. A’Hearn et al., 1995), though on the high activity end of commonly detected comets (Cochran et al., 2012).

2.1. In situ study of the neutral gas coma

The study of the neutral gas coma and its composition is of prime importance to understand the origin of the ices on the nucleus. On CI this is addressed by the Mass Analyzer for Neutrals in a Coma (MANiaC) instrument on S/C A. MANiaC uses a gauge to measure gas density and a time-of-flight mass spectrometer to analyze composition (Jones et al., 2024).

The duration of the neutral gas measurements on a trajectory with flyby distance $R_{CA,A}$, i.e., the time period T_n during which the gas density n_n is above the sensitivity limit of the instrument ($n_{0,MANiaC} = 10^3 \text{ molecules cm}^{-3}$ for the time-of-flight mass spectrometer (Jones

Table 1
Physical quantities.

Quantity	Symbol	Units
<i>comet parameters</i>		
cometocentric distance	R	km
closest approach	R_{CA}	km
flyby speed	u_{flyby}	km s ⁻¹
radius of the nucleus	R_{nucleus}	km
gas production rate per unit area	ϵ_n	molecules m ⁻² s ⁻¹
<i>neutral gas instrument</i>		
neutral gas production rate	Q_{gas}	molecules s ⁻¹
neutral gas density	n_n	molecules m ⁻³
neutral gas density detection limit	$n_{0,\text{MANiAC}}$	molecules m ⁻³
neutral gas detection distance	R_n	km
time for neutral observations	T_n	s
neutral expansion velocity	u_n	km s ⁻¹
<i>plasma instruments</i>		
H ₂ O ionization rate	ν	s ⁻¹
in/outbound bow shock distance	$R_{\text{BS1}}, R_{\text{BS2}}$	km
time inside bow shock	T_{BS}	s
diamagnetic cavity radius	R_{DC}	km
time inside diamagnetic cavity	T_{DC}	s
in/outbound mass loading distance	$R_{\text{ML1}}, R_{\text{ML2}}$	km
time inside mass loading region	T_{ML}	s
<i>dust instrument</i>		
dust production rate	Q_{dust}	kg s ⁻¹
dust-to-gas mass ratio	δ_{DG}	
dust expansion velocity	u_{dust}	km s ⁻¹
dust mass spectrum	T_m	kg ⁻¹
masses of spectral breaks	$m_0, \zeta m_0$	kg
dust mass spectrum exponents	μ_1, μ_2	
relevant dust particle mass	m_{dust}	kg
relevant dust mass fraction	α_{dust}	
relevant dust particle number density	n_{dust}	m ⁻³
relevant dust particle column density	N_{dust}	m ⁻²
instrument cross-section	S_{dust}	m ²
detected number of particles	N_{dust}	
<i>remote sensing instruments^a</i>		
camera resolution	γ_{rs}	rad pixel ⁻¹
number of pixels of nucleus image	N_{rs}	pixel
distance with nucleus > 1 pixel	R_{rs}	km
observation duration (pointing)	$T_{\text{point,rs}}$	s
observation duration (fixed)	$T_{\text{fixed,rs}}$	s
<i>critical dust impact risk^b</i>		
critical dust particle impact energy	$\mathcal{E}_{\text{crit}}$	J
critical dust particle mass	m_{crit}	kg
critical dust mass fraction	α_{crit}	
critical dust particle number density	n_{crit}	m ⁻³
critical dust particle column density	N_{crit}	m ⁻²
S/C cross-section	S_{SC}	m ²
critical number of particles	N_{crit}	
<i>science return and survival probability^{b,c}</i>		
probability density of q	$P(q)$	
science return function for q	$\phi(q)$	
science return from instruments	F_{instr}	
weights for instruments	w_{instr}	
weights for S/C	w_{SC}	
weights for pre- and post-CA parts	$w_{\text{pre}}, w_{\text{post}}$	
survival probability for instrument on S/C	$G_{\text{instr,SC}}$	
survival probability for S/C	G_{SC}	
data acquisition probability for S/C	I_{SC}	
expected science return for S/C	H_{SC}	
expected science return for CI	H_{CI}	

^a Subscript “rs” = CoCa, MIRMIS, NAC, WAC, HI, OPIC, EnVisS.

^b Subscript “SC” = A, B1, B2.

^c Subscript “instr” = any instrument.

et al., 2024)), can be computed from

$$T_n = \frac{2}{u_{\text{flyby}}} \sqrt{\frac{Q_{\text{gas}}}{4\pi u_n n_{0,\text{MANiAC}}} - R_{\text{CA,A}}^2} \quad (2)$$

with gas production rate Q_{gas} , neutral gas expansion speed u_n , and flyby velocity u_{flyby} , assuming spherically symmetric gas production, the absence of an extended gas source, and an adequate correction for the S/C background (Schläppi et al., 2010).

The signal-to-noise ratio $n_n/n_{0,\text{MANiAC}}$ changes during the flyby as it rises to a peak value $n_n(R_{\text{CA,A}})/n_{0,\text{MANiAC}}$ at closest approach and back to zero on the outbound part of the flyby trajectory, if gas production stays constant during the flyby. To be able to distinguish the contributions of minor species, the peak density must exceed the background by several orders of magnitude. For instance, one of the stated ambitions is to measure the D/H ratio (Jones et al., 2024), which requires a density contrast of 10^4 (Altwegg et al., 2015).

Taking into account measurement duration and maximum signal-to-noise ratio, the observation quality for the neutral gas measurements is defined here as

$$q_{\text{gas}} = T_n \log_{10} \frac{n_n(R_{\text{CA,A}})}{n_{0,\text{MANiAC}}} \quad (3)$$

Defining $T_n^* = 1$ h of continuous observations as being a reasonable basis for success, with 4 orders of magnitude contrast at closest approach, the reference is $q_{\text{gas}}^* = 4 \times 1$ h.

2.2. In situ study of the plasma environment

The study of the comet plasma environment involves multiple aspects. To properly understand the configuration of the induced magnetosphere, one must know the state of the solar wind during the flyby, which can be assessed from observations before and after the flyby. Upstream of the bow shock, there is the pick-up region which itself is of scientific interest. Important plasma boundaries, such as the diamagnetic cavity boundary and the bow shock (or a “bow wave” or “infant bow shock” (Gunell et al., 2018) for less active comets), offer insights into the dynamics of the solar wind–comet magnetosphere interaction (see, e.g. Goetz et al., 2022). Whether these regions and boundaries are observed, depends on the size of the comet magnetosphere and the flyby distance. The regions tend to be larger closer to the Sun, where the comet is more active and the ionization rate is higher. The dynamic ranges of the plasma instruments are designed to be usually sufficient for the different regions involved. There might be difficulties with the ionospheric density becoming too high near CA so that some instruments are saturated; this aspect has not been included in our assessment of plasma observation quality but can be verified after the trade-off R_{CA} has been found. The model proposed by Timar et al. (2017), based on the interplay between gas production and solar wind pressure, is used to estimate the size of the diamagnetic cavity, R_{DC} , and the time T_{DC} spent therein. The in- and outbound extent of the mass-loading region, R_{ML1} and R_{ML2} , the bow shock positions R_{BS1} and R_{BS2} , and the time durations during which the S/C are immersed in the mass-loading region, T_{ML} , and inside the bow shock, T_{BS} , can be computed from models (Koenders et al., 2013; Edberg et al., 2023; De Keyser et al., 2024) and are a function of the gas production rate, the ionization rate, the solar wind conditions, but also of the encounter geometry. Depending on the solar zenith angle at CA, the duration from the inbound bow shock crossing to CA may differ strongly from the time span from CA to the outbound crossing, but T_{BS} and T_{ML} do not sensitively depend on the orientation of the trajectory relative to the comet. The computations presented here have been performed for a solar zenith angle at CA of 30°. The following quality indicators are proposed:

$$q_{\text{ML}} = T_{\text{ML}}, \quad q_{\text{BS}} = T_{\text{BS}}, \quad q_{\text{DC}} = T_{\text{DC}}, \quad (4)$$

with $q_{\text{BS}}^* = T_{\text{BS}}^* = T_n^*$, $q_{\text{ML}}^* = 5T_{\text{BS}}^*$, and $q_{\text{DC}}^* = T_{\text{BS}}^*/100$ as the corresponding reference values.

Plasma sensors are present on S/C A as part of the DFP-A instrument suite (magnetometer, ion and electron spectrometers, Langmuir probes, passive and active plasma wave sensor), probe B1 carries the HI instrument (magnetometer, ion mass spectrometer), and probe B2 has the

DFP-B2 magnetometer (Jones et al., 2024). Because of mass and power constraints the instrument packages on B1 and B2 are limited, with the only type of sensor present on all three S/C being a magnetometer.

2.3. In situ study of the dust environment

A spherically symmetric dust coma is considered, with a dust density n_{dust} that varies with the inverse square cometocentric distance (i.e., no trapped dust population, no particles reflected by solar radiation pressure). The DISC dust instrument on CI measures impacting dust grains with momentum in the range 5×10^{-11} – 5×10^{-4} N s (particles with higher momentum are counted, but their mass cannot be determined accurately) corresponding to a mass range of 10^{-15} – 10^{-8} kg (Della Corte et al., 2023; Jones et al., 2024).

The dust particle mass spectrum $\mathcal{F}_m(m)$ is approximated here by a combination of power laws, based on Rosetta observations of the 67P dust environment (Rotundi et al., 2015); see the Appendix for more details. It is assumed that the spectrum retains the same shape with cometocentric distance, although one can expect some changes as the dust particles progressively lose their volatile content and may break apart. Since v_{flyby} is much larger than the dust speed relative to the nucleus, the momentum distribution has the same shape as the mass distribution. The number of particles in the DISC momentum range constitute a mass fraction α_{dust} of the total dust mass as given by Eq. (40) in Appendix. For simplicity, these particles are described here by a single representative dust mass bin m_{dust} given by Eq. (41). If the dust particles stream away from the nucleus with speed u_{dust} , their number density is

$$n_{\text{dust}} = \frac{\alpha_{\text{dust}} Q_{\text{dust}}}{4\pi u_{\text{dust}} m_{\text{dust}} R^2} \quad (5)$$

with Q_{dust} the dust mass produced per unit time. Since $u_{\text{dust}} \ll v_{\text{flyby}}$, the number of dust particles N_{dust} in the relevant mass bin that are scooped up by the instrument per unit cross-section is obtained by integrating n_{dust} along the trajectory. Hence, the number of particles recorded by an instrument with exposed cross-section S_{dust} is

$$\mathcal{N}_{\text{dust}} = S_{\text{dust}} N_{\text{dust}} = \frac{S_{\text{dust}} \alpha_{\text{dust}} Q_{\text{dust}}}{4u_{\text{dust}} m_{\text{dust}} R_{\text{CA}}} \quad (6)$$

This provides a computationally cheap method to evaluate the dust particle number, which in the context of this statistical study is preferred above more sophisticated models, such as the Engineering Dust Coma Model (Marschall et al., 2022).

For the DISC momentum range one obtains $\alpha_{\text{dust}} = 0.1$ from Eq. (40) and $m_{\text{dust}} = 2.5 \times 10^{-9}$ kg from Eq. (41), as the break in the mass spectrum is at $m_0 = 5 \times 10^{-7}$ kg assuming a mass density of 1 g cm^{-3} (see Appendix). The DISC dust collection area is $S_{\text{dust}} = 84 \text{ mm} \times 84 \text{ mm}$ (Jones et al., 2024). For the reference mission to a moderately active comet with a water-dominated coma and a dust-to-gas mass ratio $\delta_{\text{DG}}^* = 2$ (McDonnell et al., 1991), the dust production rate is $Q_{\text{dust}}^* = 3000 \text{ kg s}^{-1}$. For a flyby distance $R_{\text{CA,A}}^* = 1000 \text{ km}$, the expected number of dust grains registered on S/C A is $\mathcal{N}_{\text{dust}}^* \approx 200$ if one assumes $u_{\text{dust}} = 1 \text{ m s}^{-1}$. Recording a high number of particles is scientifically interesting but if there are too many, the odds that a larger particle would damage the instrument are significant. DISC is present on both S/C A and probe B2. As $R_{\text{CA,B2}} < R_{\text{CA,A}}$, the number of detected particles becomes higher, and so does the risk of a fatal dust particle hit.

Taking as observation quality indicator the quantity $q_{\text{dust}} = \mathcal{N}_{\text{dust}}$, one finds

$$\frac{q_{\text{dust}}}{q_{\text{dust}}^*} = \frac{\mathcal{N}_{\text{dust}}}{\mathcal{N}_{\text{dust}}^*} = \frac{Q_{\text{dust}} v_{\text{flyby}}^{2/3} R_{\text{CA}}^*}{Q_{\text{dust}}^* v_{\text{flyby}}^{*2/3} R_{\text{CA}}}, \quad (7)$$

where the instrument-specific proportionality factors disappear, at least if u_{dust} does not change with activity. Depending on v_{flyby} , the DISC momentum range corresponds to a different part of the mass spectrum and thus to a different expectation for the number of particles that is collected. Note that it is implicitly assumed here that $v_{\text{flyby}} m_0$ always remains within the DISC momentum range.

2.4. Remote sensing of nucleus and near-comet environment

Remote sensing of the nucleus benefits from approaching the nucleus up close, allowing to resolve smaller spatial structures on its surface. During a very close flyby, exposure times must remain short to avoid motion blur if the flyby is also a fast one, depending on whether the camera can follow the moving target; it is assumed here that CA is sufficiently far away.

A large nucleus permits interesting data to be taken already from far away. For a given flyby distance, a larger nucleus will fill a bigger part of the field of view. Depending on the flyby speed and on the rotation rate of the nucleus, imaging can cover a larger fraction of the nucleus surface and its 3D shape can be better determined.

Nucleus size can be inferred from nucleus brightness and an assumed albedo well in advance of the flyby. Another option, which is followed here, is to assume that comet activity is roughly proportional to illuminated area,

$$Q_{\text{gas}} = \epsilon_n \pi R_{\text{nucleus}}^2, \quad (8)$$

where ϵ_n is the average gas production rate per unit surface (for a spherical nucleus) at 1 au. Since 1P/Halley has $R_{\text{nucleus}} \approx 5 \text{ km}$ (Reinhard, 1986), a value $\epsilon_n = 6.4 \times 10^{21} \text{ molecules m}^{-2} \text{ s}^{-1}$ is found. It is thus possible to infer R_{nucleus} from Q_{gas} , which should give a reasonable order of magnitude. For a reference activity 1/10th that of 1P/Halley, one finds $R_{\text{nucleus}}^* = 1.6 \text{ km}$. This matches the situation at 67P reasonably well, with $Q_{\text{gas}} = 3 \times 10^{28} \text{ molecules m}^{-2} \text{ s}^{-1}$ at 1.24 au (Hansen et al., 2016) and a nucleus measuring $4.3 \times 2.6 \times 2.1 \text{ km}$ (Jorda et al., 2016).

The Comet Camera (CoCa) on S/C A sports a resolution of $\gamma_{\text{CoCa}} = 8 \mu\text{rad pixel}^{-1}$ (Jones et al., 2024). The image of a spherical nucleus at CA has

$$N_{\text{CoCa}} = \pi \left(\frac{R_{\text{nucleus}}}{\gamma_{\text{CoCa}} R_{\text{CA,A}}} \right)^2 = \frac{Q_{\text{gas}}}{\gamma_{\text{CoCa}}^2 \epsilon_n R_{\text{CA,A}}^2} \quad (9)$$

pixels (if $R_{\text{nucleus}} \ll R_{\text{CA,A}}$). For a comet with the reference activity, $N_{\text{CoCa}}^* \approx 0.12 \text{ Mpixel}$ while the detector has 3 Mpixel, so the nucleus and inner coma out to 5 comet radii fill the field of view.

The distance within which the comet nucleus is more than 1 pixel across is

$$R_{\text{CoCa}} = \sqrt{\frac{Q_{\text{gas}}}{\gamma_{\text{CoCa}}^2 \epsilon_n}}, \quad (10)$$

which scales linearly with R_{nucleus} ; for the reference case one finds $R_{\text{CoCa}}^* = 3.5 \times 10^5 \text{ km}$. The time during which sensible nucleus images can be taken, then is

$$\begin{aligned} T_{\text{point,CoCa}} &= \frac{2}{v_{\text{flyby}}} \sqrt{R_{\text{CoCa}}^2 - R_{\text{CA,A}}^2} \\ &\approx \frac{2R_{\text{CoCa}}}{v_{\text{flyby}}} \propto \frac{\sqrt{Q_{\text{gas}}}}{v_{\text{flyby}}}. \end{aligned} \quad (11)$$

Note that usually $R_{\text{CoCa}} \gg R_{\text{CA,A}}$, so that $T_{\text{point,CoCa}}$ is essentially independent of $R_{\text{CA,A}}$. CoCa can continuously image the target thanks to the Rotating Mirror Assembly (RMA), which points to the nucleus throughout the flyby, while S/C A maintains a constant attitude with its dust shield facing the ram direction. From the CoCa point of view, an encounter with the reference comet at $v_{\text{flyby}}^* = 50 \text{ km s}^{-1}$ would result in $T_{\text{point,CoCa}}^*$ being about 4 h. Outside that time period CoCa can still observe the inner dust coma (though at low resolution) so that the useful observation time may be longer. A CoCa remote sensing observation quality parameter is constructed by including both the duration and the best achievable resolution,

$$q_{\text{CoCa}} = N_{\text{CoCa}} T_{\text{point,CoCa}}, \quad (12)$$

so that

$$\frac{q_{\text{CoCa}}}{q_{\text{CoCa}}^*} = \frac{Q_{\text{gas}}^{3/2} R_{\text{CA,A}}^{*2} v_{\text{flyby}}^*}{Q_{\text{gas}}^{*3/2} R_{\text{CA,A}}^2 v_{\text{flyby}}}, \quad (13)$$

which no longer depends on the specific CoCa properties.

The Modular InfraRed Molecules and Ices Sensor (MIRMIS) on S/C A consists of three infrared sensors (Jones et al., 2024). Its performance depends on the spatial resolution and the duration of the observations, so that $q_{\text{MIRMIS}} \propto q_{\text{CoCa}}$ and $q_{\text{MIRMIS}}/q_{\text{MIRMIS}}^* = q_{\text{CoCa}}/q_{\text{CoCa}}^*$. This is a simplification that disregards MIRMIS scanning mirror speed limitations.

The Narrow Angle Camera (NAC) on probe B1 has a fixed look direction. It has an angular resolution of $\gamma_{\text{NAC}} = 19 \mu\text{rad pixel}^{-1}$ (Jones et al., 2024). For a fixed B1 orientation, it images the nucleus as it moves through its $3.5^\circ \times 2.6^\circ$ field of view. Near CA and looking perpendicular to the ram direction, this happens in a matter of seconds as

$$T_{\text{fixed,NAC}} = \frac{2}{v_{\text{flyby}}} R_{\text{CA,B1}} \tan \frac{\phi}{2} \quad (14)$$

with ϕ the width of the field of view traversed by the comet. NAC thus provides a snapshot of the nucleus. As observation quality parameter, it is appropriate to consider

$$q_{\text{NAC}} = N_{\text{NAC}}, \quad (15)$$

from which

$$\frac{q_{\text{NAC}}}{q_{\text{NAC}}^*} = \frac{Q_{\text{gas}} R_{\text{CA,B1}}^{*2}}{Q_{\text{gas}}^* R_{\text{CA,B1}}^2}. \quad (16)$$

The Wide Angle Camera (WAC) on B1 has a $90^\circ \times 90^\circ$ field of view ($\gamma_{\text{WAC}} = 770 \mu\text{rad pixel}^{-1}$). Therefore $T_{\text{fixed,WAC}}$, with $\phi = 90^\circ$, amounts to tens of seconds to minutes, but WAC will benefit from B1 attitude manoeuvres to collect observations over a longer time period. A reasonable observation quality parameter is

$$q_{\text{WAC}} = N_{\text{WAC}} T_{\text{fixed,WAC}}, \quad (17)$$

(or a multiple thereof) from which

$$\frac{q_{\text{WAC}}}{q_{\text{WAC}}^*} = \frac{Q_{\text{gas}} R_{\text{CA,A}}^* v_{\text{flyby}}^*}{Q_{\text{gas}}^* R_{\text{CA,A}} v_{\text{flyby}}}. \quad (18)$$

The Hydrogen Imager on probe B1 observes the spatial distribution of Hydrogen in the inner coma (Ly- α observations at 121.6 nm) with a Cassegrain telescope with $4.2^\circ \times 4.2^\circ$ field of view ($\gamma_{\text{HI}} = 350 \mu\text{rad pixel}^{-1}$). Also taking advantage of the B1 reorientations, the useful time is a multiple of $T_{\text{fixed,HI}}$. The observation quality is defined as

$$q_{\text{HI}} = N_{\text{HI}} T_{\text{fixed,HI}}, \quad (19)$$

so that

$$\frac{q_{\text{HI}}}{q_{\text{HI}}^*} = \frac{q_{\text{WAC}}}{q_{\text{WAC}}^*}. \quad (20)$$

The Optical Periscopic Imager for Comets (OPIC) on probe B2 offers nucleus and inner coma images from far away with its forward looking periscope ($\gamma_{\text{OPIC}} = 155 \mu\text{rad pixel}^{-1}$). In this case, there is much value in the fact that its observations commence well before CA, so that the useful time is a multiple of $T_{\text{point,OPIC}}$, with early coma views but little or no nucleus image resolution. The nucleus is lost from the $18.2^\circ \times 18.8^\circ$ field of view centered on the forward direction shortly before CA, at which time the periscope mirror moves out of the way, allowing the nucleus to be imaged once every spin period. The observation quality can be considered proportional to the total duration of the observations and to the nucleus resolution (or the resolution of inner coma features), so that

$$q_{\text{OPIC}} = N_{\text{OPIC}} T_{\text{point,OPIC}}, \quad (21)$$

from which

$$\frac{q_{\text{OPIC}}}{q_{\text{OPIC}}^*} = \frac{Q_{\text{gas}}^{3/2} R_{\text{CA,B2}}^{*2} v_{\text{flyby}}^*}{Q_{\text{gas}}^{*3/2} R_{\text{CA,B2}}^2 v_{\text{flyby}}}. \quad (22)$$

Table 2

Instrument contributions to the science merit for each spacecraft.

Instrument	A	B1	B2
MANiaC	0.20		
DFP-A, PS, DFP-B2	0.20	0.33	0.25
DISC	0.20		0.25
CoCa	0.20		
MIRMIS	0.20		
NAC		0.17	
WAC		0.17	
HI		0.33	
OPIC			0.25
EnVisS			0.25

The Entire Visible Sky (EnVisS) all-sky imaging system on B2 has a science return that is not very sensitive to the actual flyby distance. Making such images from deep within the coma is one of the objectives, but neither the resolution nor the duration of the observations strongly depend on the flyby distance. A constant quality $q_{\text{EnVisS}} = q_{\text{EnVisS}}^*$ is therefore adopted.

2.5. Science return

The science return from each instrument is obtained as follows:

$$\begin{aligned} F_{\text{MANiaC}} &= \phi \left(\frac{q_{\text{gas}}}{q_{\text{gas}}^*} \right), \\ F_{\text{DFP-A}} &= \frac{1}{3} \phi \left(\frac{q_{\text{ML,A}}}{q_{\text{ML,A}}^*} \right) + \frac{1}{3} \phi \left(\frac{q_{\text{BS,A}}}{q_{\text{BS,A}}^*} \right) + \frac{1}{3} \phi \left(\frac{q_{\text{DC,A}}}{q_{\text{DC,A}}^*} \right), \\ F_{\text{PS}} &= \frac{1}{3} \phi \left(\frac{q_{\text{ML,B1}}}{q_{\text{ML,B1}}^*} \right) + \frac{1}{3} \phi \left(\frac{q_{\text{BS,B1}}}{q_{\text{BS,B1}}^*} \right) + \frac{1}{3} \phi \left(\frac{q_{\text{DC,B1}}}{q_{\text{DC,B1}}^*} \right), \\ F_{\text{DFP-B2}} &= \frac{1}{3} \phi \left(\frac{q_{\text{ML,B2}}}{q_{\text{ML,B2}}^*} \right) + \frac{1}{3} \phi \left(\frac{q_{\text{BS,B2}}}{q_{\text{BS,B2}}^*} \right) + \frac{1}{3} \phi \left(\frac{q_{\text{DC,B2}}}{q_{\text{DC,B2}}^*} \right), \\ F_{\text{DISC-A}} &= \phi \left(\frac{q_{\text{dust,A}}}{q_{\text{dust,A}}^*} \right), \\ F_{\text{DISC-B2}} &= \phi \left(\frac{q_{\text{dust,B2}}}{q_{\text{dust,B2}}^*} \right), \\ F_{\text{rs}} &= \phi \left(\frac{q_{\text{rs}}}{q_{\text{rs}}^*} \right), \end{aligned}$$

with rs = CoCa, MIRMIS, NAC, WAC, HI, OPIC, and EnVisS.

The overall science return per spacecraft is a weighted combination of the contributions of all instruments,

$$F_{\text{SC}} = \sum_{\text{instr}} w_{\text{instr,SC}} F_{\text{instr}}, \quad (23)$$

for SC = A, B1, B2, and where $\sum_{\text{instr}} w_{\text{instr,SC}} = 1$, ensuring that $F_{\text{total}} \in [0, 1]$. The chosen instrument weights are given in Table 2. While their values are somewhat arbitrary, this choice balances the different types of measurement. The outcome of the optimization is not very sensitive to the exact values.

2.6. Dust risk

The spacecraft is exposed to high-speed comet dust impacts during the flyby, the effects of which can be dramatic (Jones et al., 2024). The spacecraft design helps to mitigate the risk but it cannot be completely eliminated. A dust hit may perturb S/C attitude, depending on the particle momentum and the place where it hits (Haslebacher et al., 2022). Another possibility is that dust impacts with an energy above a critical value $\mathcal{E}_{\text{crit}}$ perforate the dust shield and destroy S/C subsystems. The focus here is on the second type of failure where particles with a mass exceeding

$$m_{\text{crit}} = \frac{2\mathcal{E}_{\text{crit}}}{v_{\text{flyby}}^2} \quad (24)$$

cause fatal damage. From Eq. (6), and with S_{SC} the S/C cross-section, the number of critical impacts is

$$\mathcal{N}_{crit} = \frac{S_{SC} \alpha_{crit} Q_{dust}}{4u_{dust} m_{crit} R_{CA}}. \quad (25)$$

Computing \mathcal{N}_{crit} from this expression requires \mathcal{E}_{crit} to be known. Its value, however, depends on unknown properties of the impacting particle and of the mechanical spacecraft structure. Using the expression from Eq. (42) for the mass fraction α_{crit} of particles with mass $> m_{crit}$, one finds

$$\frac{\mathcal{N}_{crit}}{\mathcal{N}_{crit}^*} = \frac{Q_{dust} m_{crit}^{*4/3} R_{CA}^*}{Q_{dust}^* m_{crit}^{*4/3} R_{CA}} = \frac{Q_{dust} v_{flyby}^{8/3} R_{CA}^*}{Q_{dust}^* v_{flyby}^{*8/3} R_{CA}}, \quad (26)$$

with \mathcal{N}_{crit}^* the number of critical particles for the reference conditions, showing how the number of critical impacts strongly depends on the flyby speed. One can obtain \mathcal{N}_{crit} from

$$\mathcal{N}_{crit} = \mathcal{N}_{crit}^* \left(\frac{\mathcal{N}_{crit}}{\mathcal{N}_{crit}^*} \right) \quad (27)$$

if one specifies the value of \mathcal{N}_{crit}^* , the risk for a fatal S/C hit in the reference case.

The survival probability of the spacecraft can in general be written as

$$G_{SC} = e^{-\mathcal{N}_{crit}}. \quad (28)$$

If $\mathcal{N}_{crit} \ll \mathcal{N}_{crit}^*$, the survival probability is close to 100%. With $\mathcal{N}_{crit} = \mathcal{N}_{crit}^*$, the survival probability corresponds to the one specified for the reference conditions. For higher $\mathcal{N}_{crit}/\mathcal{N}_{crit}^*$ the survival chances decrease rapidly.

The survival probabilities of the different S/C for the reference scenario should reflect the different possible failure modes. Here, S/C A is assumed to have a 99.5% survival probability for the reference scenario, so that $\mathcal{N}_{crit,A}^* = 0.005$. As a rough estimate, this would correspond to a critical mass of ~ 5 g, which could vaporize ~ 0.5 kg of S/C material. Note that for Halley-type activity, the risk is 10 \times higher, i.e., 95% survival probability. Since for B1

$$\frac{\mathcal{N}_{crit,B1}}{\mathcal{N}_{crit,A}} = \frac{S_{B1} \alpha_{crit,B1} m_{crit,A} R_{CA,A}}{S_A \alpha_{crit,A} m_{crit,B1} R_{CA,B1}} \quad (29)$$

$$= \frac{S_{B1} R_{CA,A}}{S_A R_{CA,B1}} \left(\frac{\mathcal{E}_{crit,A}}{\mathcal{E}_{crit,B1}} \right)^{\frac{4}{3}}, \quad (30)$$

one finds $\mathcal{N}_{crit,B1}^* = 0.012$ because $S_{B1} \approx 0.25$ m² and $S_A \approx 2.56$ m² (Jones et al., 2024), and because the dust shielding on S/C A is more efficient, expressed here by $\mathcal{E}_{crit,B1}/\mathcal{E}_{crit,A} = 0.1$. Similarly, with $S_{B2} = S_{B1}$ and $\mathcal{E}_{crit,B2} = \mathcal{E}_{crit,B1}$, one finds $\mathcal{N}_{crit,B2}^* = 0.026$. Probes B1 and B2 thus have a survival probability that is lower than that of S/C A, despite being smaller.

Apart from the risk to the S/C, there is the risk to the instruments. Most of them have a sensor that necessarily is exposed to the ambient environment and therefore very sensitive to dust hits, while their data processing unit is well-protected. Therefore, if an instrument sensor takes a fatal hit, the data recorded up to that moment are not lost. To simplify the risk analysis, each instrument sensor is considered to be 5 \times as vulnerable as the S/C on which it is hosted. This cannot be entirely correct as the survival probability of a sensor may scale differently than that of its host, since it may be sensitive to a different part of the dust mass spectrum. The risk also depends on instrument size. Sensors may have different mechanical resistance against impacts (e.g. Della Corte et al., 2025), which may lead to differences in risk scaling too. The instrument survival probability is

$$G_{instr} = e^{-5\mathcal{N}_{crit}}. \quad (31)$$

As the dust coma is assumed to be spherically symmetric, the survival probabilities for the time spent either before or after CA are equal, with $G_{instr,pre} = G_{instr,post} = \sqrt{G_{instr}}$ and $G_{pre,SC} = G_{post,SC} = \sqrt{G_{SC}}$.

3. Trade-off methodology

Armed with these estimates of science return and of instrument and S/C risk, a number of comet flyby scenarios has been studied for different flyby distances.

3.1. Parameters

The analysis is set up for the typical situation where one has to decide on a choice of the flyby distance a few months or weeks before the actual flyby. At that moment, the heliocentric distance of the flyby is known; in the example studied hereafter it is taken to be 1 au. The solar zenith angle at closest approach is defined once the S/C trajectory to the target comet has been defined. A value of 30 $^\circ$ is adopted here. The flyby velocity v_{flyby} is also known once the S/C trajectory is defined. S/C A is assumed to perform its flyby in the plane defined by the Sun–comet line and v_{flyby} with closest approach occurring after passing through the noon meridian ($\psi_{CA} = 30^\circ$). To keep things simple, the neutral gas outflow velocity $u_n = 1$ km s⁻¹ is deemed constant, although in reality it may vary somewhat with the gas production rate.

For several other parameters only estimates are available, so that a range of values has to be considered.

- The gas production rate can be predicted with modest precision. Apart from time variations, there may be spatial structure such as the day/night difference; small-scale spatial inhomogeneity in surface outgassing is washed out at typical flyby distances. We assume Q_{gas} has a lognormal distribution around the estimated value, with a 1 σ spread of 25%. Values of 10²⁷–10²⁹ molecules s⁻¹ are the most likely for CI (De Keyser et al., 2024).
- It is hard to properly estimate the dust-to-gas ratio δ_{DG} (Choukroun et al., 2020; Laurent-Varin et al., 2024). A lognormal distribution is considered here, with a 1 σ spread of 50% around the estimated value (ensuring a range of values of more than an order of magnitude), from which one obtains $Q_{dust} = \delta_{DG} Q_{gas}$. The reasoning is as follows. The production of OH or of CN, both of which correlate to within 15% (Cochran et al., 2012), can be obtained from spectroscopic observations from Earth. Both directly relate to the water production. By using the typical volatile composition, and noting that water is the most abundant constituent, the (diurnally averaged) Q_{gas} can be estimated with 20% uncertainty or better. Dust coma brightness $Af\rho$ is found from observations with a precision of a few % or better (e.g. Garcia et al., 2020; Gillan et al., 2024). However, the conversion of $Af\rho$ to Q_{dust} is very sensitive to the dust properties and their size spectrum (Fink and Rubin, 2012; Garcia et al., 2020; Gillan et al., 2024; Marschall et al., 2022). There are several ways to constrain the dust properties, e.g., by ratioing $Af\rho$ values at different wavelengths to obtain the mass spectrum power law index (Haslebacher et al., 2024), by exploiting spectropolarimetric measurements to infer a characteristic dust size and porosity (Kwon et al., 2022), or by analyzing infrared spectra (Lellouch et al., 1998). The dust production rate can then be determined within an order of magnitude (Marschall et al., 2022) or better. Anticipating detailed ground-based studies of the target comet, a δ_{DG} estimate with a 1 σ uncertainty of 50% should be available before the flyby. This estimate can be extrapolated to the moment of encounter as δ_{DG} changes only slowly with time (e.g. Marschall et al., 2020, Fig. 11), except if the flyby would happen to occur exactly at the time of a change of seasons or in case of a nucleus break-up; for an encounter near 1 au, there is no need to worry about dust outbreaks associated with the onset of sublimation of hypervolatiles that occur at large heliocentric distances.

- The ionization rate ν at 1 au varies with the solar UV flux. A lognormal distribution is used around the estimated value with a 1σ spread of 5%. It is assumed that the gas coma is water-dominated and that photo-ionization of water molecules is the principal ionization channel. The average value $\nu(1\text{ au}) = 3\text{--}7 \times 10^{-7} \text{ s}^{-1}$ depends on solar activity (Huebner and Mukherjee, 2015), but there can be significant short-term variability.
- Solar wind conditions change continuously at time scales from seconds to years. The approach of De Keyser et al. (2024) is reused here to compute T_{DC} , T_{BS} and T_{ML} , in which solar wind properties are randomly chosen between those of slow and fast wind (with slow wind 3 times more likely than fast wind), while following empirical scaling laws.

3.2. Analysis for a single spacecraft

For each R_{CA} , a large number of encounters has been simulated. For the parameters for which only a range is known, parameter values are generated according to the probability distribution. For each simulated encounter, the science return and the survival probabilities are determined, giving a net return

$$H_{\text{SC}} = F_{\text{SC}} \Gamma_{\text{SC}} \quad (32)$$

with the data acquisition probability

$$\Gamma_{\text{SC}} = G_{\text{SC}} (w_{\text{pre,SC}} \sqrt{G_{\text{instr,SC}}} + w_{\text{post,SC}} G_{\text{instr,SC}}), \quad (33)$$

for SC = A, B1, B2. Quantities $w_{\text{pre,SC}}$ and $w_{\text{post,SC}}$ reflect the contributions of the pre- and post-CA parts:

$$w_{\text{pre,A}} = w_{\text{pre,B1}} = 0.5 (1 + \sin \psi_{\text{CA}}) \quad (34)$$

$$w_{\text{post,A}} = w_{\text{post,B1}} = 0.5 (1 - \sin \psi_{\text{CA}}) \quad (35)$$

$$w_{\text{pre,B2}} = 0.9 (1 + \sin \psi_{\text{CA}}) \quad (36)$$

$$w_{\text{post,B2}} = 0.1 (1 - \sin \psi_{\text{CA}}). \quad (37)$$

Equal weight is given to both if $\psi_{\text{CA}} = 0^\circ$, at least for A and B1, with $w_{\text{pre}} + w_{\text{post}} = 1$. For B2, the post-CA part is smaller, reflecting the limited fraction of battery life foreseen for this part ($w_{\text{pre}} + w_{\text{post}} < 1$ in this case). If $\psi_{\text{CA}} > 0^\circ$, i.e., if the CA happens after passing through the noon meridian, the inbound trajectory receives more weight. This is justified for the in situ instruments, as the most interesting aspects of the solar wind–comet interaction occur upstream. It is also appropriate for the remote sensing instruments, as they observe a larger illuminated part of the comet prior to CA. The converse is true if CA happens before passing through noon. Eq. (32) combines the weighted science return with the survival probabilities in a simplified manner. Pre-CA science is considered acquired when the sensor survives the first part of the encounter and the S/C the entire encounter, with probability $\sqrt{G_{\text{instr,SC}}} G_{\text{SC}}$, while post-CA science requires surviving both the in- and outbound parts, with probability $G_{\text{instr,SC}} G_{\text{SC}}$, since both the sensor and the spacecraft must survive the entire encounter. Note that an asymmetry appears with respect to the sign of ψ_{CA} : passing through noon prior to CA allows to collect more relevant data with less risk.

Collecting the results from the individual simulations, one obtains the probability distribution functions for the science return, the survival probabilities, and the net return for that particular R_{CA} . In a final step, the percentiles of the distribution of H_{SC} are examined to find out for which R_{CA} the net return is maximum.

3.3. Analysis for a multi-spacecraft mission

S/C A, B1, and B2 are designed for given survival probabilities at their nominal flyby distances. Different flyby distances can be considered but in the present study they are scaled together as the risk is proportional to $1/R_{\text{CA}}$, so that the relative survival probabilities $G_{\text{B1}}/G_{\text{A}}$ and $G_{\text{B2}}/G_{\text{A}}$ remain the same.

Starting from the net return for the three spacecraft, a measure of mission success can be defined as follows:

$$H_{\text{CI}} = w_{\text{A}} H_{\text{A}} + w_{\text{B1}} H_{\text{B1}} G_{\text{A}} + w_{\text{B2}} H_{\text{B2}} G_{\text{A}}, \quad (38)$$

with $w_{\text{A}} + w_{\text{B1}} + w_{\text{B2}} = 1$, so that $H_{\text{CI}} \in [0, 1]$. S/C A plays a special role since it acts as a data relay for B1 and B2. S/C A, B1, and B2 perform measurements at a high data rate so that transmitting them to Earth in real time is impossible; a store-and-forward approach is used (Jones et al., 2024). If S/C A fails during the encounter, the data from B1 and B2 is lost, which is why G_{A} is a factor in the last 2 terms of H_{CI} . A destruction of B1 or B2 near CA should not be regarded as a complete failure: They are designed to be expendable (their inbound data are recorded by S/C A, and most of B2's battery power is consumed before CA anyway). This is partially taken into account by giving B1 and B2 less weight. The choice $w_{\text{A}} = 0.50$, $w_{\text{B1}} = 0.25$, $w_{\text{B2}} = 0.25$ has been made here.

A multi-spacecraft mission must offer more than the sum of the three individual spacecraft. This is especially true for CI, where simultaneous in situ measurements are expected to provide insight in the 3-dimensional structure of the coma. With the above formulation, it is clear that maximizing H_{CI} requires the 3 S/C to survive together (G_{A} , G_{B1} , G_{B2} all close to 1) so that the multi-spacecraft aspect is guaranteed.

The mission analysis can be performed by examining the percentiles of the distribution of H_{CI} and finding the R_{CA} -values for which the net return is maximum.

4. Results

In this section the trade-off between science return and risk is illustrated for a flyby whose estimated characteristics are the reference parameters, i.e., $Q_{\text{gas}} = 5 \times 10^{28} \text{ molecules s}^{-1}$, $\delta_{\text{DG}} = 2$, $\nu = 5 \times 10^{-7} \text{ s}^{-1}$, and $v_{\text{flyby}} = 50 \text{ km s}^{-1}$. Thereafter, it is shown how the optimal flyby distance depends on the different parameters.

4.1. Science return

The single- and multi-spacecraft analysis has been carried out by performing Monte Carlo experiments, 5000 times simulating a flyby with values sampled from the log-normal distributions for Q_{gas} , ν , and δ_{DG} , as explained in Section 3.1. Fig. 2 shows the resulting probability distribution functions for the various physical quantities that determine the science return for gas, plasma, dust, and remote sensing measurements for S/C A, B1, and B2, and for the reference flyby distances.

The distribution of Q_{gas} values is reflected by the spread on the obtained values of R_{n} and the corresponding T_{n} . S/C A can study the neutral gas above the detection limit during ~ 40 minutes on average, which is not far from the T_{n}^* that is hoped for. Like Q_{gas} , $n_{\text{n}}(R_{\text{CA}})$ has a log-normal distribution. The neutral gas densities at closest approach seen by S/C A are around $4 \times 10^6 \text{ cm}^{-3}$, implying a signal-to-noise ratio of 4000. By stacking spectra, determining the D/H ratio should be possible.

The diamagnetic cavity extends out to 400 km on average for the assumed Q_{gas} and solar wind property ranges. The diamagnetic cavity boundary would be observed by A and B1 in roughly a quarter of the cases, while the probability to see it with B2 is about 50%. B2 typically stays inside the cavity for up to a few tens of seconds. The inbound bow shock crossing by S/C A takes place at 50000 km from the comet on average; the outbound crossing is a few times farther out. This results in a median stay of about an hour inside the induced magnetosphere, similar to the 21P/Giacobini-Zinner and 19P/Borrelly flybys (Edberg et al., 2023), but $P(T_{\text{BS}})$ does show a large spread. In 6% of the cases, the dwell time inside the bow shock is less than 5 minutes. In fact, there is a 10% probability of not even entering into the comet's induced magnetosphere at all. Conversely, $T_{\text{BS}} > 10000 \text{ s}$ has a 17% probability. The distributions are slightly altered for probe B1 and B2.

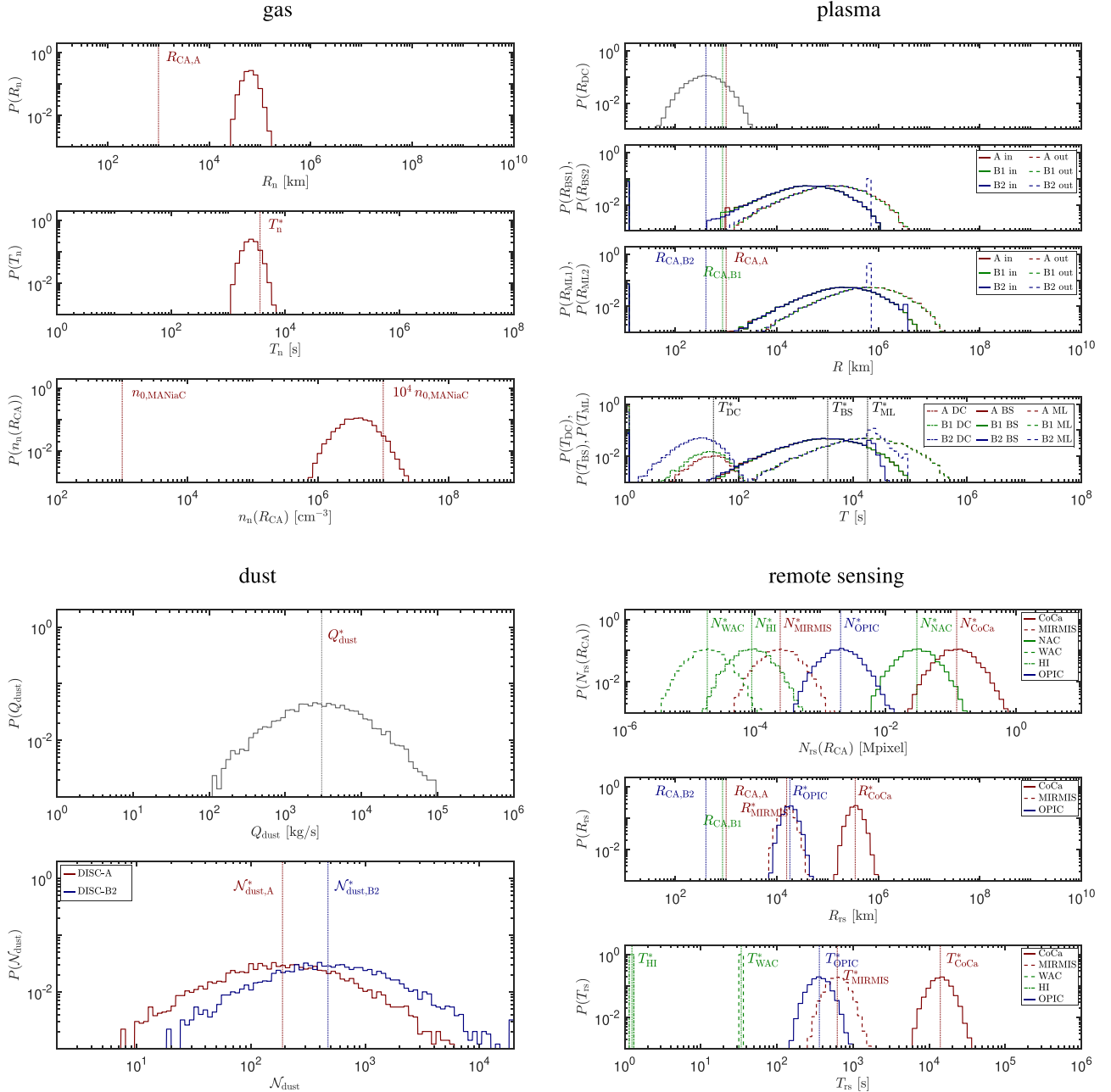


Fig. 2. Probability distributions for neutral gas, plasma, dust, and remote sensing observations for a 50 km s⁻¹ flyby at 1000 km, 850 km, and 400 km CA distance for S/C A, B1, and B2, of a comet with $Q_{\text{gas}} = 5 \times 10^{28}$ molecules s⁻¹ and $\delta_{\text{DG}} = 2$, and ionization rate $\nu = 5 \times 10^{-7}$ s⁻¹ at 1 au. Note that some curves may overlap.

In principle, S/C A may already be inside the bow shock when the probes are released, but this does not seem to be the case as the $P(R_{\text{BS1}})$ curves for A, B1 and B2 all coincide, except at the low end where the distributions are cut off at the respective R_{CA} . Because of the finite probe lifetime and limited ISL range, the effective end of observation by B1 and B2 may occur before their outbound bow shock crossing. From the cutoff of $P(R_{\text{BS2}})$ just below 10⁶ km for B2 and the lack thereof for B1, it is apparent that the finite B2 battery lifetime implies a premature end of plasma observations, making it impossible to detect a far-out outbound bow shock. This does not happen for B1, which is assumed to always remain within the ISL range in the simulations. This explains the peak in $P(T_{\text{BS}})$ for B2, while there is no such peak for B1. Similar conclusions can be drawn for the crossings into and out of the mass-loading region, 5× farther out than the bow shock (De Keyser et al., 2024). In this case, however, there is a cutoff at the high end in $P(R_{\text{ML1}})$ for B2 (not for B1) indicating that there are situations where the entry

into the mass loading region occurs between the B1 and B2 release. The peak in the $P(R_{\text{ML2}})$ distribution for B2 is at the same position as in $P(R_{\text{BS2}})$, both being due to the probe's end of life. This explains the shape of the T_{ML} distribution for B2. There is a considerable spread on the estimated time spent inside the bow shock and mass-loading region, due to uncertainties on Q_{gas} , ν , and the solar wind conditions.

The dust production rate shows a log-normal distribution as it results from the product of two log-normal variables. It is centered around 3000 kg s⁻¹ assuming the gas coma consists entirely of water; uncertainty and variability regarding the neutral composition would add an additional spread. The distribution of the number of grains recorded by the dust instrument tends to be very broad. Comparing DISC-A and DISC-B2, the number is seen to scale with $1/R_{\text{CA}}$. Note that the number of dust particles estimated here is computed by binning all the particles into a single mass bin. Taking into account the actual distribution, the number of particles can be a multiple of that but with

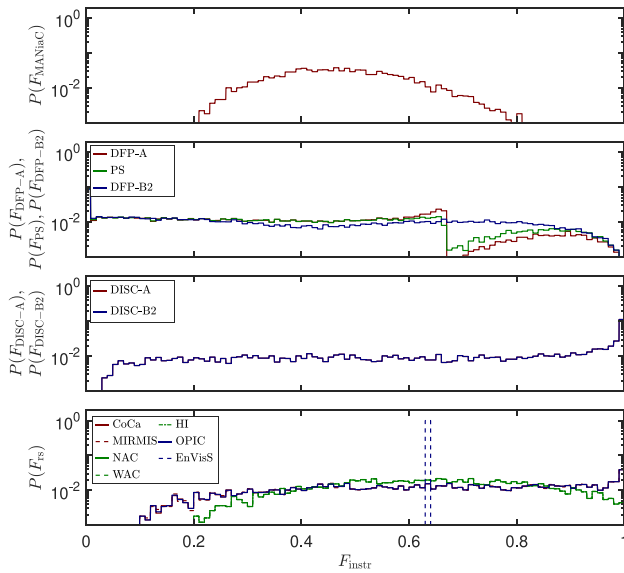


Fig. 3. Probability distributions for the science return of neutral gas, plasma, dust, and remote sensing observations, for a 50 km s^{-1} flyby at 1000 km, 850 km, and 400 km CA distance for S/C A, B1, and B2, of a comet with $Q_{\text{gas}} = 5 \times 10^{28}$ molecules s^{-1} and $\delta_{\text{DG}} = 2$, and an ionization rate $\nu = 5 \times 10^{-7} \text{ s}^{-1}$ at 1 au. Note that some curves may overlap.

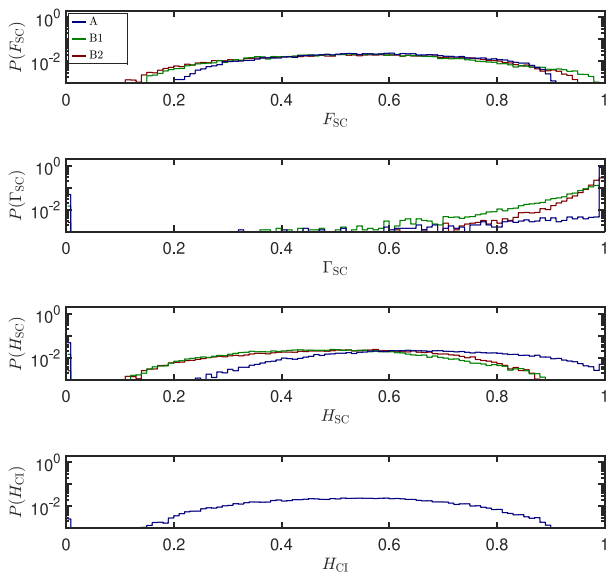


Fig. 4. Probability distributions for the S/C science return, S/C data acquisition probability, expected S/C science return and expected mission return, for a 50 km s^{-1} flyby at 1000 km, 850 km, and 400 km CA distance for S/C A, B1, and B2, of a comet with $Q_{\text{gas}} = 5 \times 10^{28}$ molecules s^{-1} and $\delta_{\text{DG}} = 2$, and an ionization rate $\nu = 5 \times 10^{-7} \text{ s}^{-1}$ at 1 au.

predominantly lower mass particles.

CoCa would observe a reference scenario nucleus that fills 4% of the image at CA on S/C A. The nucleus is visible as more than a single pixel within a distance of $4 \times 10^5 \text{ km}$. This lasts for $1.4 \times 10^4 \text{ s}$. NAC on B1 produces a nucleus image that covers about 0.03 Mpixel, corresponding to a linear spatial resolution that is $2 \times$ coarser despite B2 getting closer. The other remote sensing instruments produce lower resolution images, while HI and WAC in particular aim at imaging the inner coma rather than the nucleus itself. All these quantities are computed with the hypothesis that outgassing is proportional to the illuminated nucleus surface area; uncertainties on this scaling should be added to the results shown here.

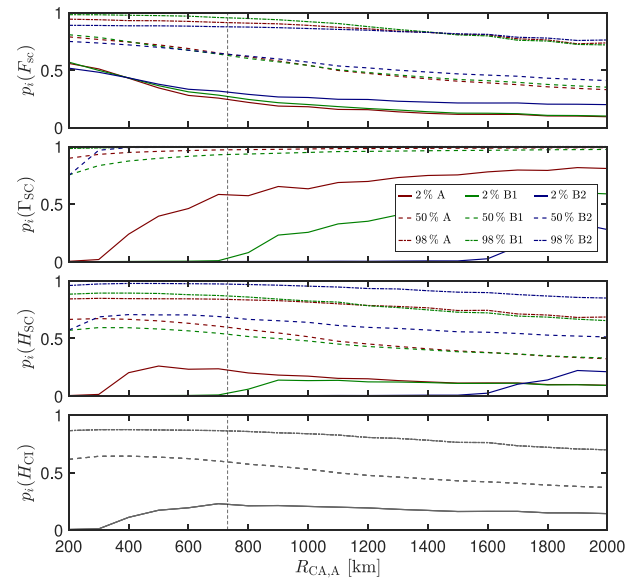


Fig. 5. Trade-off between science return and risk. From top to bottom: 2%, 50%, and 98% percentiles of the S/C science return, data acquisition probability, expected S/C science return and expected mission science return, obtained for the same conditions as Figs. 2 and 3 but for a range of flyby distances. The horizontal axis gives the flyby distance of S/C A; the flyby distances of B1 and B2 are scaled correspondingly.

Given the results reported in Fig. 2, the probability distributions of the science return values for the different instruments are obtained (Fig. 3). It is not surprising that the return for all types of measurements is reasonable (>0.2) to very good (>0.8), except for the plasma measurements that show a wide spread, a relative paucity of values of $F_{\text{DFP-A}}$ and F_{PS} immediately above $2/3$ corresponding to situations where A and B1 do not enter into the diamagnetic cavity, and even a poor return (<0.1) in 20% of the situations (when the bow shock is not even crossed).

As defined here, the science return probability distribution $P(F_{\text{SC}})$ is similar for A, B1 and B2 (Fig. 4, top). The data acquisition probability distribution $P(G_{\text{SC}})$ (Fig. 4, 2nd panel) reflects the fatal impact risks on sensors and on the spacecraft as outlined in Section 2.6; the data acquisition probability is rather high for B2 because of the low weight given to the post-CA data. The expected S/C science return H_{SC} combines both science return and risk (Eq. (32)), and results in distributions with a lower return. High science return is linked to strong comet activity, which implies higher risk, which is why H_{SC} values close to 1 are improbable (unless for B2, which is considered expendable). The probability distribution of the expected mission science return H_{CI} computed from Eq. (38) (Fig. 4, bottom) indicates that, for the reference flyby, a reasonable overall science return is expected.

4.2. Flyby distance trade-off

The analysis of the previous section can be repeated for flyby distances $R_{\text{CA,A}} = 200 \text{ km}, 300 \text{ km}, \dots, 2000 \text{ km}$, with $R_{\text{CA,B1}}$ and $R_{\text{CA,B2}}$ being scaled correspondingly. For each set of flyby distances, the probability distributions of the S/C science return, the S/C data acquisition probability, the expected S/C science return and the expected mission science return are computed. The percentiles at the 2%, 50%, and 98% levels of these distributions are plotted in Fig. 5. While the science return decreases with R_{CA} , the data acquisition probability increases. Consequently, both for the individual S/C and for the mission as a whole, there exists a sweet spot where the expected science return is maximum.

The optimal flyby distance trade-off is performed here for the 2% percentile, i.e., the situation in which the actual mission science return

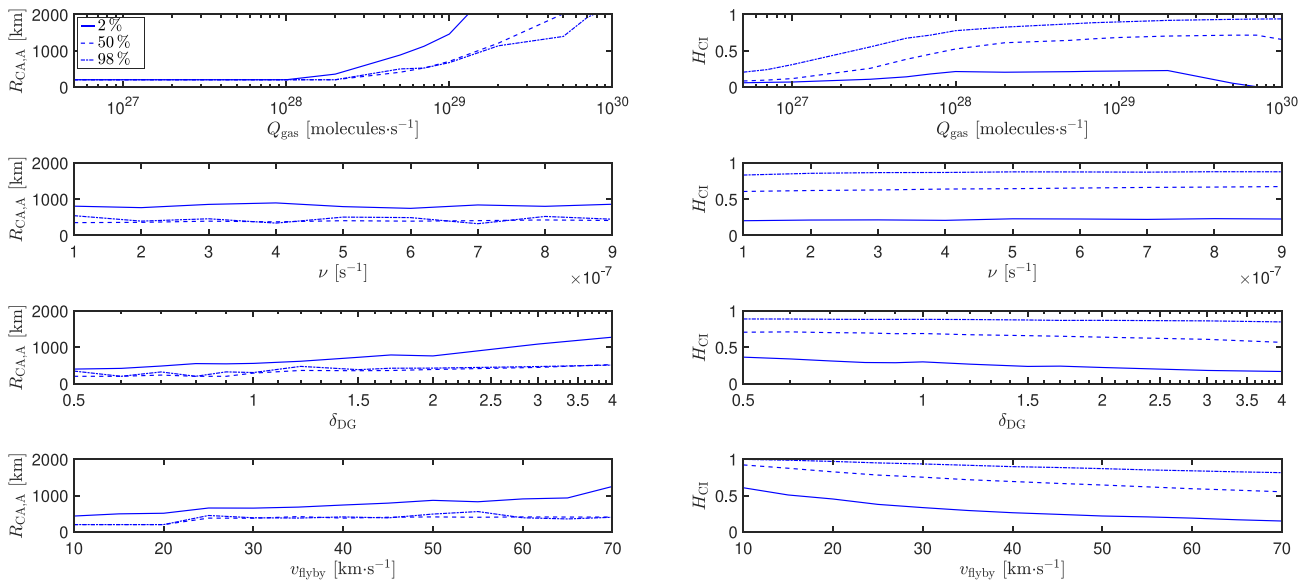


Fig. 6. Left: Variation of the optimum flyby distance based on the 2%, 50%, and 98% percentiles with (from top to bottom) gas production rate, ionization rate, dust-to-gas ratio, and flyby speed. Right: Corresponding values of the expected mission science return.

is higher than this value in 98% of the cases. The maximum of $p_{2\%}(H_{CI})$ is obtained as the maximum of a smooth linear spline fit of the values computed at the discrete set of $R_{CA,A}$ flyby distances. This optimum flyby distance for S/C A of about 730 km (620 km for B1, 290 km for B2) is marked by a vertical dashed line in Fig. 5. Since $p_{2\%}(H_{CI})$ is relatively flat near its maximum, the optimum is not sharply defined. The role of the weights attributed to the S/C is not negligible. Maintaining the relative scaling of the flyby distances of the different spacecraft is not strictly necessary. Relaxing that requirement can improve the mission return as more free parameters are introduced in the optimization problem. In view of the simplified description of the science return used here, doing so may not be justified. Note that the optimum distance depends on the percentile considered.

4.3. Variation of flyby distance with main parameters

The dependence of the optimum flyby distance on the main parameters has been studied to highlight the underlying trends. The results are reported in Fig. 6.

First, the gas production rate is varied over the range expected for the CI target. The optimum flyby distance is found to increase with Q_{gas} , which is due to the fact that Q_{dust} and thus the dust impact risk increase as well. At first, the science return at the optimum flyby distance improves as the comet is more active, because there is more neutral gas, a larger induced magnetosphere, and a larger nucleus to be studied. But from a certain point on, the safe distance from the comet is so far away that the science return diminishes. The optimum comet activity for CI is found to be in the range 10^{28} – 10^{29} molecules s^{-1} .

Changes in the ionization rate ν affect only the plasma measurements. Since these already show a large spread, e.g., due to the role of solar wind variability, there is only a small improvement of the overall science return as the induced magnetosphere is expected to become larger on average, while there is no effect on the risk.

More dramatic are changes in the dust-to-gas ratio, since these directly affect the dust flux and hence the risk. The optimum flyby distance increases with δ_{DG} and the science return degrades, because the neutral gas, plasma, and nucleus characteristics do not change.

Dust particle impact energy depends on v_{flyby}^2 . High flyby speeds are therefore much more risky than low flyby speeds and thus require a larger flyby distance. Moreover, a slow flyby allows the neutral gas, plasma and remote sensing instruments to obtain more data, thus improving the science return.

5. Discussion and conclusions

In this study a methodology has been described that allows to compute the optimal closest approach distance for a comet flyby mission. It has been applied to the case of Comet Interceptor. The relatively simple technique can be employed in the weeks prior to the flyby to tune the flyby distance so as to minimize the dust impact risk and to maximize the science output, benefiting from the known flyby speed and the best available estimates of the comet activity, the dust-to-gas ratio, and the ionization rate at that moment in time. Although a flyby at 1 au has been considered here, the procedure can easily be applied for a flyby anywhere in the 0.9 to 1.2 au range that is accessible to CI (Jones et al., 2024).

The analysis relies on several approximations. There are simplifications in the description of the science return:

- The science return from the instruments is judged from just a few parameters. Ideally, one may attempt to define the science return based on the mission’s science requirements but not all of these requirements are easily quantifiable, nor is their relative importance defined.
- The bow shock stand-off distance and the size of the diamagnetic cavity are quite variable as they depend on solar wind pressure. The present analysis considers random solar wind conditions that remain fixed throughout the flyby, and thus it ignores the associated plasma boundary motion. This is especially the case for slower flyby speeds, for which the solar wind is sampled over a longer time period. Therefore, the chances of crossing the bow shock or entering into the diamagnetic cavity may be underestimated.
- Similarly, the gas production rate may vary with time and thus the ionospheric density, also leading to changes in plasma boundary positions during the flyby.
- The science return of the remote sensing instruments is based on a simple proportionality between gas production rate and illuminated surface. This may be a crude approximation, but it is reasonable within the snow line.
- Several effects of v_{flyby} have not been included in the analysis, such as the secondary electrons produced by neutral impacts on the spacecraft (affecting the plasma instruments), the influence of flyby speed on the impact fragmentation of molecules (relevant for MANiaC), and the amount of ionization produced by dust

impacts (used by the DFP-A/COMPLIMENT Langmuir probes for nanodust detection).

- The description of the science return does not include technical constraints such as the limited scanning rate of the RMA and OPIC mirrors that matters when the flyby is too close and/or too fast, thermal constraints due to the orientation with respect to Sun and Earth, limits on the telemetry when the flyby takes place close to the Sun as seen from Earth, etc. The delivery error, i.e., the finite precision on the trajectory determination and corrections, prohibits too close flybys, as one then effectively loses control over the risk as it sharply increases near the nucleus. Large flyby distances imply large separations between S/C A and B1/B2 that may exceed the ISL range. Therefore, one must verify a posteriori whether the trade-off described in this paper satisfies all technical constraints and the flyby scenario must be adapted accordingly.

There are also important simplifications in the risk model:

- To evaluate the dust risk, a realistic dust mass distribution has been used but this remains uncertain; see the Appendix for a more detailed discussion.
- The dust risk does not account for spatially or temporally variable dust emission. To be on the safe side, one can perform the analysis with a worst-case δ_{DG} .
- The fatal impact risk of the sensors has been considered to be $5\times$ higher than that of the platform they are located on, which avoids the need for instrument dust impact risk models but is not very precise.
- S/C survival has been linked here to dust particle impact energy. The consequences of attitude control perturbations due to impact momentum have not been considered.

Despite these shortcomings, the model captures the essence of the problem. All in all, the proposed methodology offers a handy tool to determine the optimal flyby distance. It definitely shows that having the flexibility of targeting flyby distances between a few hundred and ~ 2000 km is very useful.

The methodology can also play a role in the target comet selection process. The mission science return at the optimal flyby distance is best for a slow flyby of a moderately active comet (10^{28} – 10^{29} molecules s^{-1}) with low dust-to-gas ratio, preferably closer to the Sun where the ionization rate is largest. Selecting a comet with activity $< 10^{28}$ molecules s^{-1} leads to a poor science return for the neutral gas and plasma instruments, while choosing a very active one forces the spacecraft to stay > 2000 km from the nucleus (Fig. 6, top left). The methodology can be used to compare flyby scenarios at different potential targets, once an intercepting trajectory has been designed and screened for technical feasibility. At the time of selection, the targets are likely still far from the Sun and uncertainties on their gas production rate and dust-to-gas ratio are large, which may limit the usefulness of such a comparison.

CRediT authorship contribution statement

J. De Keyser: Writing – review & editing, Writing – original draft, Visualization, Validation, Supervision, Software, Resources, Project administration, Methodology, Investigation, Funding acquisition, Formal analysis, Conceptualization. **N.J.T. Edberg:** Writing – review & editing, Validation, Methodology, Conceptualization. **P. Henri:** Writing – review & editing, Supervision. **H. Rothkaehl:** Writing – review & editing, Project administration. **V. Della Corte:** Writing – review & editing. **M. Rubin:** Writing – review & editing. **R. Funase:** Writing – review & editing. **S. Kasahara:** Writing – review & editing. **C. Snodgrass:** Writing – review & editing.

Declaration of competing interest

The authors declare that they have no known competing financial interests or personal relationships that could have appeared to influence the work reported in this paper.

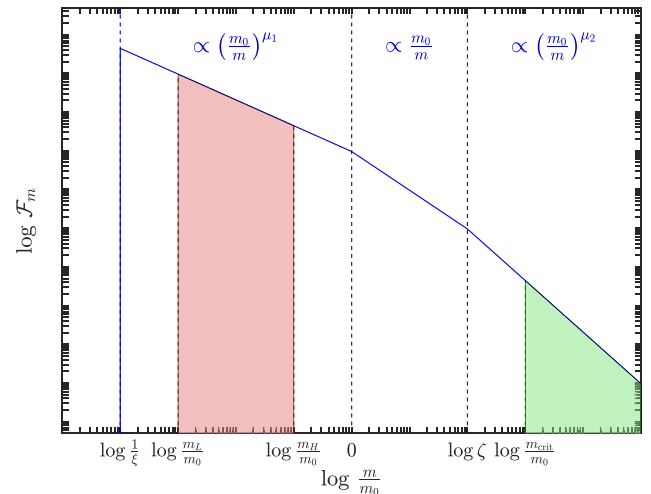


Fig. 7. Dust mass spectrum. See main text for a detailed explanation.

Acknowledgments

Work by JDK has been supported by the Belgian Science Policy Office through ESA PRODEX PEA 4000139830. NE was supported by SNSA grant 2021-00047. Work by MR was funded by the Canton of Bern and the Swiss National Science Foundation (SNSF 200020_207312). French co-authors acknowledge the support of CNES to the Comet Interceptor mission. Italian co-authors acknowledge the support of ASI to the Comet Interceptor mission with ASI-INAF agreements 2020-4-HH.0 and 2023-14-HH.0. The software used for this work is freely available from De Keyser (2024).

Appendix

Dust particles are a subject of scientific investigation but also the cause of impact damage sustained by the spacecraft and/or its instruments during the flyby. The dust spectrum considered here is a combination of power laws as shown in Fig. 7. Below a reference mass m_0 , the differential dust particle number flux is $\propto 1/m^{\mu_1}$, with $\mu_1 < 1$. In an intermediate mass range $m_0 \leq m < \zeta m_0$, the differential flux is $\propto 1/m$. Above ζm_0 , the differential number flux is $\propto 1/m^{\mu_2}$ with $\mu_2 > 1$. This spectrum is inspired by the Rosetta measurements reported by Rotundi et al. (2015, Fig. 2), who observed $\mu_1 \approx 2/3$ for grain diameters of tens to hundreds of microns, but a $1/m$ distribution for mm-sized particles. The power law exponent $\mu_2 > 1$ is necessary to make the spectrum integrable. Below mass m_0/ξ , at the nanometer-scale, no dust particles are to be found. This spectrum can be expressed as

$$\begin{aligned}
 F_m &= 0 & m < m_0/\xi \\
 &= F_{m_0} \left(\frac{m_0}{m}\right)^{\mu_1} & m_0/\xi \leq m < m_0 \\
 &= F_{m_0} \frac{m_0}{m} & m_0 \leq m < \zeta m_0 \\
 &= F_{m_0} \zeta^{\mu_2-1} \left(\frac{m_0}{m}\right)^{\mu_2} & \zeta m_0 \leq m
 \end{aligned} \tag{39}$$

with

$$F_{m_0} = \frac{Q_{\text{dust}}}{m_0[(1-\xi^{\mu_1-1})/(1-\mu_1) + \log \zeta + 1/(\mu_2-1)]} \approx \frac{Q_{\text{dust}}}{9m_0},$$

where the numerical value is obtained for $\mu_1 = 2/3$, $\mu_2 = 4/3$ and $\zeta = e^3 \approx 20$, and noting that $\xi \gg 1$. The exact shape of the low-mass part of the spectrum does not really matter as it contributes a negligible mass fraction.

The dust detector momentum range $[p_L, p_H]$ is assumed to be always in the range $[m_0 v_{\text{flyby}}/\xi, m_0 v_{\text{flyby}}]$, for all flyby velocities considered here. The mass fraction in the detector range (shaded red region in

Fig. 7) is

$$\alpha_{\text{dust}} = \int_{p_L/v_{\text{flyby}}}^{p_H/v_{\text{flyby}}} F_m dm / Q_{\text{dust}} \approx \frac{1}{3} \left(\frac{p_H}{m_0 v_{\text{flyby}}} \right)^{1/3}. \quad (40)$$

which depends on v_{flyby} . The representative mass is

$$m_{\text{dust}} = \int_{p_L/v_{\text{flyby}}}^{p_H/v_{\text{flyby}}} F_m m dm / \int_{p_L/v_{\text{flyby}}}^{p_H/v_{\text{flyby}}} F_m dm \approx \frac{p_H}{4v_{\text{flyby}}}. \quad (41)$$

The critical dust particle mass is assumed to be always $> \zeta m_0$, for all v_{flyby} values considered. The corresponding mass fraction (shaded green region in Fig. 7) is

$$\alpha_{\text{crit}} = \frac{1}{3} \left(\frac{\zeta m_0}{m_{\text{crit}}} \right)^{1/3}, \quad (42)$$

where $m_{\text{crit}} = 2\mathcal{E}_{\text{crit}}/v_{\text{flyby}}^2$ depends on the flyby velocity.

Below, this model is compared to the EDCM (Marschall et al., 2022) and ComMoDe models (Reynier et al., 2024).

First, it is used to determine $\mathcal{N}_{\text{dust}}$ to estimate the performance of the dust instrument. Rather than the absolute number of particles, the present paper is interested in how $\mathcal{N}_{\text{dust}}$ scales with the parameters. The scaling with Q_{dust} is linear, as is the case for the EDCM and ComMoDe. The scaling with v_{flyby} is more complicated as the flyby velocity defines the momentum of the particles and thus which fraction of the mass distribution is seen by DISC. The shape of the mass spectrum matters. The model described above uses distinct mass ranges, with exponent 2/3 for the DISC mass range, i.e., a size spectrum exponent -2 , while EDCM and ComMoDe use a single power law with size spectrum exponent -3.2 to -4.5 , which is steeper. In short, with respect to the dust instrument, the steeper spectrum of EDCM and ComMoDe would lead to more smaller particles in the relevant mass range. That means that for larger v_{flyby} , the number of detected particles would increase faster than with the above model, as many more small particles enter the DISC momentum range from the lower end than there are particles that leave it at the upper end.

The second and more important role of the dust model is in determining the likelihood of being hit by a particle with mass $> m_{\text{crit}}$, at the high mass end of the power law. Mass spectrum exponent $\mu_2 = -4/3$ corresponds to a size spectrum exponent -4 , while the EDCM uses size spectrum exponents -3.2 to -4.5 . Therefore, the scaling of the dust flux with v_{flyby} is very similar (idem for ComMoDe which follows the EDCM). What might be different is the coefficient of the power law. However, by rescaling the number of critical particles to a specified survival probability, the role of that coefficient is removed. In short, with respect to fatal dust impacts, there is no fundamental difference between the present model, EDCM or ComMoDe.

Note that in the present paper, only flybys mostly located on the sunward side are considered, for which the assumption of a quasi-spherical dust coma should not differ substantially from EDCM and ComMoDe.

Data availability

This paper does not rely on data. The code underlying the results is shared at <https://doi.org/10.18758/nn9g6vno>.

References

A'Hearn, M.F., Millis, R.C., Schleicher, D.G., Osip, D.J., Birch, P.V., 1995. The ensemble properties of comets: Results from narrowband photometry of 85 comets, 1976–1992. *Icarus* 118 (2), 223–270. <http://dx.doi.org/10.1006/icar.1995.1190>.
A'Hearn, M.F., et al., 2005. Deep Impact: Excavating Comet Tempel 1. *Science* 310 (5746), 258–264. <http://dx.doi.org/10.1126/science.1118923>.
A'Hearn, M.F., et al., 2011. EPOXI at comet Hartley 2. *Science* 332 (6036), 1396–1400. <http://dx.doi.org/10.1126/science.1204054>.
Altwegg, K., Balsiger, H., Bar-Nun, A., et al., 2015. 67P/Churyumov-Gerasimenko, a Jupiter family comet with a high D/H ratio. *Science* 347, 1261952. <http://dx.doi.org/10.1126/science.1261952>.

Boice, D.C., et al., 2000. The Deep Space 1 encounter with comet 19P/Borrelly. *Earth, Moon, Planets* 89, 301–324. <http://dx.doi.org/10.1023/A:1021519124588>.
Brandt, J.C., et al., 1985. The International Cometary Explorer (ICE) mission to comet Giacobini-Zinner (G/Z). In: Carusi, A., Valsecchi, G.B. (Eds.), *Dynamics of Comets: Their Origin and Evolution*. Springer Netherlands, Dordrecht, pp. 405–414. http://dx.doi.org/10.1007/978-94-009-5400-7_35.
Brownlee, D., et al., 2006. Comet 81P/Wild 2 under a microscope. *Science* 314 (5806), 1711–1716. <http://dx.doi.org/10.1126/science.1135840>.
Choukroun, M., Altwegg, K., Kühr, E., et al., 2020. Dust-to-gas and refractory-to-ice mass ratios of comet 67P/Churyumov-Gerasimenko from Rosetta observations. *Space Sci. Rev.* 216, 44. <http://dx.doi.org/10.1007/s11214-020-00662-1>.
Cochran, A., Barker, E., Gray, C., 2012. Thirty years of cometary spectroscopy from McDonald Observatory. *Icarus* 218 (1), 144–168. <http://dx.doi.org/10.1016/j.icarus.2011.12.010>.
De Keyser, J., 2024. Optimal choice of closest approach distance for a comet flyby: Supplementary material - software. <http://dx.doi.org/10.18758/nn9g6vno>.
De Keyser, J., Edberg, N.J.T., Henri, P., et al., 2024. In situ plasma and neutral gas observation time windows during a comet flyby: Application to the Comet Interceptor mission. *Planet. Space Sci.* 244, 105878. <http://dx.doi.org/10.1016/j.pss.2024.105878>.
Della Corte, V., Ferretti, S., Piccirillo, A.M., Rotundi, A., Bertini, I., Cozzolino, F., Ferone, A., Fiscale, S., Longobardo, A., Inno, L., Ammannito, E., Sindoni, G., Grappasonni, C., Sylvest, M., Patel, M.R., Ertel, H., Millinger, M., Rothkaehl, H., 2025. Performance assessment of an innovative light and compact dust shield for DISC onboard Comet Interceptor/ESA space probes. *Int. J. Impact Eng.* 195, 105146. <http://dx.doi.org/10.1016/j.ijimpeng.2024.105146>.
Della Corte, V., et al., 2023. DISC - the dust impact sensor and counter on-board Comet Interceptor: Characterization of the dust coma of a dynamically new comet. *Adv. Space Res.* 71 (8), 3457–3467. <http://dx.doi.org/10.1016/j.asr.2023.01.049>.
Edberg, N.J.T., et al., 2023. Scale size of cometary bow shocks. *Astron. Astrophys.* <http://dx.doi.org/10.1051/0004-6361/202346566>.
Fink, U., Rubin, M., 2012. The calculation of $Af\rho$ and mass loss rate for comets. *Icarus* 221 (2), 721–734. <http://dx.doi.org/10.1016/j.icarus.2012.09.001>.
Garcia, R., Gil-Hutton, R., Garcia-Migani, E., 2020. Observational results for five short-period and five long-period comets. *Planet. Space Sci.* 180, 104779. <http://dx.doi.org/10.1016/j.pss.2019.104779>.
Gillan, A.F., Fitzsimmons, A., Denneau, L., Siverd, R.J., Smith, K.W., Tonry, J.L., Young, D.R., 2024. Dust Production Rates in Jupiter-family Comets: A Two Year Study with ATLAS Photometry. *Planetary Sci. J.* 5 (1), 25. <http://dx.doi.org/10.3847/PSJ/ad1394>.
Goetz, C., et al., 2022. The plasma environment of comet 67P/Churyumov-Gerasimenko. *Space Sci. Rev.* 216, 65. <http://dx.doi.org/10.1007/s11214-022-00931-1>.
Gunell, H., et al., 2018. The infant bow shock: a new frontier at a weak activity comet. *Astron. Astrophys.* 619, L2. <http://dx.doi.org/10.1051/0004-6361/201834225>.
Hansen, K.C., et al., 2016. Evolution of water production of 67P/Churyumov-Gerasimenko: An empirical model and a multi-instrument study. *Mon. Not. R. Astron. Soc.* 462, S491–S506. <http://dx.doi.org/10.1093/mnras/stw2413>.
Haslebacher, N., Gerig, S.-B., Thomas, N., Marschall, R., Zakharov, V., Tubiana, C., 2022. A numerical model of dust particle impacts during a cometary encounter with application to ESA's Comet Interceptor mission. *Acta Astronaut.* 195, 243–250. <http://dx.doi.org/10.1016/j.actaastro.2022.02.023>.
Haslebacher, N., Thomas, N., Marschall, R., 2024. Spectral ratioing of $Af\rho$ to constrain the dust particle size distribution of comets. *Planet. Space Sci.* 248, 105925. <http://dx.doi.org/10.1016/j.pss.2024.105925>.
Huebner, W.F., Mukherjee, J., 2015. Photoionization and photodissociation rates in solar and blackbody radiation fields. *Planet. Space Sci.* 106, 11–45. <http://dx.doi.org/10.1016/j.pss.2014.11.022>.
Jones, G., Snodgrass, C., Tubiana, C., et al., 2024. The Comet Interceptor mission. *Space Sci. Rev.* 220 (9), <http://dx.doi.org/10.1007/s11214-023-01035-0>.
Jones, G., et al., 2019. Comet Interceptor: A mission to a dynamically new Solar System object. A Phase-2 Proposal in Response to the European Space Agency's Call for a Fast Class Mission.
Jorda, L., et al., 2016. The global shape, density and rotation of comet 67P/Churyumov-Gerasimenko from preperihelion Rosetta/OSIRIS observations. *Icarus* 277, 257–278. <http://dx.doi.org/10.1016/j.icarus.2016.05.002>.
Koenders, C., et al., 2013. Revisiting cometary bow shock positions. *Planet. Space Sci.* 87, 85–95. <http://dx.doi.org/10.1016/j.pss.2013.08.009>.
Krankowsky, D., et al., 1986. In situ gas and ion measurements at comet Halley. *Nature* 321 (Suppl 6067), 326–329. <http://dx.doi.org/10.1038/321326a0>.
Kwon, Y.G., Bagnulo, S., Markkanen, J., Agarwal, J., Kolokolova, L., Levasseur-Regourd, A.-C., Snodgrass, C., Tozzi, G.P., 2022. VLT spectropolarimetry of comet 67P: dust environment around the end of its intense southern summer. *Astron. Astrophys.* 657, A40. <http://dx.doi.org/10.1051/0004-6361/202141865>.
Laurent-Varin, J., James, T., Marty, J.-C., Jorda, L., Le Maistre, S., Gaskell, R., 2024. New gravity field of comet 67P/C-G based on Rosetta's Doppler and optical data. *Icarus* 424, 116284. <http://dx.doi.org/10.1016/j.icarus.2024.116284>.
Lellouch, E., Crovisier, J., Lim, T., Boekelele-Morvan, D., Leech, K., Hanner, M.S., Altieri, B., Schmitt, B., Trotta, F., Keller, H.U., 1998. Evidence for water ice and estimate of dust production rate in comet Hale-Bopp at 2.9 AU from the Sun. *Astron. Astrophys.* 339, L9–L12.

- Marschall, R., Markkanen, J., Gerig, S.-B., Pinzón-Rodríguez, O., Thomas, N., Wu, J.-S., 2020. The dust-to-gas ratio, size distribution, and dust fall-back fraction of comet 67P/Churyumov-Gerasimenko: Inferences from linking the optical and dynamical properties of the inner comae. *Front. Phys.* 8, 227. <http://dx.doi.org/10.3389/fphy.2020.00227>.
- Marschall, R., et al., 2022. Determining the dust environment of an unknown comet for a spacecraft flyby: the case of ESA's Comet Interceptor mission. *Astron. Astrophys.* A151. <http://dx.doi.org/10.1051/0004-6361/202243648>.
- McDonnell, J.A.M., Lamy, P.L., Pankiewicz, G.S., 1991. Physical properties of cometary dust. In: Newburn, Jr., R.L., et al. (Eds.), *In: Comets in the Post-Halley Era*, vol. 2, Kluwer, pp. 1043–1073.
- McDonnell, J.A.M., et al., 1993. Dust particle impacts during the Giotto encounter with comet Grigg-Skjellerup. *Nature* 362, 732–734. <http://dx.doi.org/10.1038/362732a0>.
- Morley, T., 1991. The Giotto encounter with comet P/Grigg-Skjellerup. *Eur. Space Agency Spec. Publ. ESA SP-326*, 87–491.
- Reinhard, R., 1986. The Giotto encounter with comet Halley. *Nature* 321, 313–318. <http://dx.doi.org/10.1038/321313a0>.
- Reynier, P., Haslebacher, N., Thomas, N., Mokhtari, O., Marschall, R., Cipriani, F., Johansson, F., Arpa, R., 2024. ComMoDE: A software for assessing dust environment during comet fly-by. In: EPSC Abstracts, Europlanet Science Congress 2024, vol. 17. pp. EPSC2024–1256. <http://dx.doi.org/10.5194/epsc2024-1256>.
- Rotundi, A., Sierks, H., Della Corte, V., et al., 2015. Dust measurements in the coma of comet 67P/Churyumov-Gerasimenko inbound to the Sun. *Science* 347, <http://dx.doi.org/10.1126/science.aaa3905>.
- Schläppi, B., et al., 2010. The influence of spacecraft outgassing on the exploration of tenuous atmospheres with in situ mass spectrometry. *J. Geophys. Res.* 115, A12313. <http://dx.doi.org/10.1029/2010JA015734>.
- Snodgrass, C., Jones, G.H., 2019. The European Space Agency's Comet Interceptor lies in wait. *Nature Comm.* 10, 5418. <http://dx.doi.org/10.1038/s41467-019-13470-1>.
- Taylor, M.G.G.T., Alexander, C., Altobelli, N., et al., 2015. Rosetta begins its comet tale. *Science* 347, 387. <http://dx.doi.org/10.1126/science.aaa4542>.
- Timar, A., et al., 2017. Modelling the size of the very dynamic diamagnetic cavity of comet 67P/Churyumov-Gerasimenko. *Mon. Not. R. Astron. Soc.* 469, S723–S730. <http://dx.doi.org/10.1093/mnras/stx2628>.
- Veverka, J., et al., 2013. Return to comet Tempel 1: Overview of Stardust-NExT results. *Icarus* 222 (2), 424–435. <http://dx.doi.org/10.1016/j.icarus.2012.03.034>.